Thermalization of photoexcited carriers in bismuth investigated by time-resolved terahertz spectroscopy and *ab initio* calculations

I. Timrov,[1] T. Kampfrath,[2,3] J. Faure,[1] N. Vast,[1] C. R. Ast,[4] C. Frischkorn,[2,3] M. Wolf,[2,3] P. Gava,[1] and L. Perfetti[1,2]

[1]*Laboratoire des Solides Irradiés, Ecole Polytechnique, CEA/DSM, CNRS UMR 7642, 91128 Palaiseau cedex, France*

[2]*Fachbereich Physik, Freie Universität Berlin, Arnimallee 14, 14195 Berlin, Germany*

[3]*Fritz-Haber-Institut der Max-Planck-Gesellschaft, Faradayweg 4-6, 14195 Berlin, Germany*

[4]*Max-Planck-Institut für Festkörperforschung, DE-70569 Stuttgart, Germany*

(Received 6 December 2011; revised manuscript received 2 March 2012; published 26 April 2012)

The charge carrier dynamics of photoexcited bismuth generates a Drude response that evolves over time. Our data show that the plasma frequency of bismuth displays an initial increase and a subsequent decay. We have performed *ab initio* calculations on bulk bismuth within the density functional theory and show that this peculiar behavior is due to local extrema in the valence and conduction bands. It follows that most of the carriers first accumulate in these extrema and reach the Fermi level only 0.6 ps after the photoexcitation.

DOI: 10.1103/PhysRevB.85.155139 PACS number(s): 78.47.jb, 78.40.Kc, 71.15.Mb, 71.18.+y

I. INTRODUCTION

Electronic and lattice motions in semimetallic materials display a rich phenomenology as coherent phonons[1] and hot-phonon generation.[2] In particular, bismuth is a reference material for the investigation of lattice dynamics in out-of-equilibrium conditions. The photoexcitation of this material generates coherent phonons which have various point group symmetries.[3,4] Time-resolved reflectivity and time-resolved x-ray diffraction show that the frequency of the totally symmetric (A_{1g}) phonon displays a large softening at high excitation densities.[3,5] The models that have been proposed within density functional theory (DFT) to explain the coherent lattice displacement have generated an ongoing controversy about the energy relaxation. Indeed, these models depend on the nonequilibrium distribution of the electronic system.[6,7] Since the latter is basically unknown, some authors assume that a complete thermalization of the electron gas occurs on a time scale shorter than the coherent phonon period.[7,8] Others suppose instead that electrons and holes thermalize on an ultrafast time scale but do not equilibrate with each other.[5,6] At this point, no experiment has had access to the carrier distribution at early times after excitation.

In principle, time-resolved photoemission is the most direct technique to monitor the electronic occupation numbers.[9] However, the high surface sensitivity of the emitted photoelectrons limits this approach. Indeed, the presence of surface states deeply modifies the electronic properties of the uppermost layers.[10] The surface turns out to be a good metal even if the bulk is semimetallic. As a consequence, the nonequilibrium distribution of the electrons may be substantially different on the surface and in the bulk. For this reason, we have investigated the dynamics of charge carriers by means of time-resolved terahertz spectroscopy. In contrast to photoelectrons, terahertz radiation can be transmitted through films of 100 nm thickness, thus probing the bulk properties of the system. Due to the low center frequency of the terahertz pulses, we mainly probe the Drude-like response of the electron-hole system, which arises from intraband transitions. It follows that terahertz spectroscopy is qualitatively different from transient reflectivity at 800 nm,[3] which is instead dominated by the interband transitions.

The mid-infrared conductivity of bismuth has been the subject of extensive work;[11,12] here we report its dynamics in the photoexcited state. In a semimetallic material like bismuth, the photoinduced increase in the number of conducting carriers generates an exceptionally large change of the dielectric function. In addition, we have found that the evolution of the plasma frequency as a function of the pump-probe delay displays nonmonotonic behavior that has no equivalence in other semimetals.[2] Using DFT calculations of the Bi band structure, we find that the complete thermalization of charge carriers takes place on a time scale longer than the period of the coherent phonons ($\simeq$0.34 ps; Ref. 3). On a shorter time scale, a considerable part of the holes and electrons created during photoexcitation populates local maxima and minima of the band structure, respectively. These excited carriers decay to the Fermi level with an inverse rate of 0.6 ps. Once the thermalization is complete, the electronic system dissipates the excess energy into the lattice with an inverse rate of $\simeq$4 ps.

The paper is organized as follows: Sec. II introduces the band and lattice structure of bismuth, Sec. III presents the terahertz measurements, and Sec. IV provides an explanation of the observed dynamics.

II. STRUCTURAL AND ELECTRONIC PROPERTIES

A. Lattice structure

Bismuth is the heaviest element among the group-V semimetals. Like As and Sb, it crystallizes in the $A7$ rhombohedral structure, which can be obtained from the simple cubic structure formed by two interpenetrating fcc sublattices. Two independent distortions are applied: a strain of the unit cell along the [111] direction, and an internal displacement of the atoms of the two fcc sublattices toward each other along the [111] direction. The resulting lattice has the trigonal symmetry and contains two atoms per unit cell, as illustrated in Fig. 1(a). More details on the $A7$ structure can be found in Ref. 15, and the group-theoretical analysis of the $A7$ structure is discussed in Ref. 16. The Brillouin zone (BZ) of bismuth is shown in Fig. 1(b).

Three parameters completely determine the unit cell and atomic positions: the length a_0 of the rhombohedral vectors,

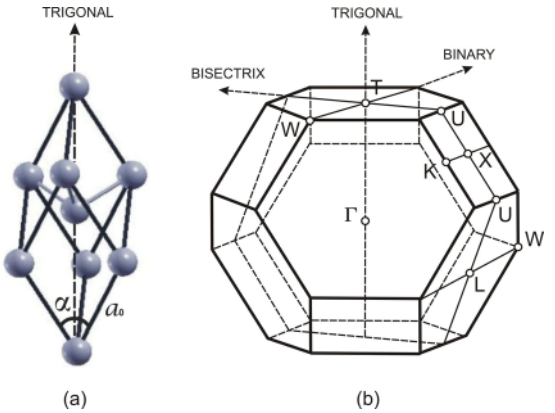

FIG. 1. (Color online) (a) *A*7 rhombohedral unit cell of bismuth. (b) Brillouin zone with the usual notation for symmetry points (Ref. 13). The principal crystallographic axes (trigonal, binary, and bisectrix) are indicated according to Ref. 14.

the rhombohedral angle α, and the internal parameter u describing atomic positions along the trigonal axis: (u,u,u) and $(-u,-u,-u)$. From x-ray diffraction measurements at a low temperature,[17] the following parameters for the unit cell of Bi are found: $a_0 = 4.7236$ Å, $\alpha = 57.35°$, and $u = 0.234$ (in units of a_0). We have performed DFT calculations of the total energy in the generalized gradient approximation (GGA) and found convergence toward an absolute minimum for the following values of the structural parameters: $a_0 = 4.9227$ Å, $\alpha = 56.36°$, and $u = 0.232$ (in units of a_0). Our value of a_0 is 4% larger than the experimental one.[17] The increase in the GGA volume is caused by the inclusion of the 5*d* electronic states in the valence bands, which has been found to greatly improve the transferability tests of the pseudopotential. The exchange and correlation functional was checked, and the local density approximation (LDA) volume turned out to equal the experimental one within 0.02%. This contradicts the usual expectation that the LDA volume is smaller than the experimental one. Inclusion of the 5*d* electrons in the valence bands thus increases both the LDA and GGA volumes.

B. Dispersion of Kohn-Sham energy levels

We have performed state-of-the-art *ab initio* calculations of the electronic structure in the framework of the DFT (Refs. 18 and 19) with the Perdew-Burke-Ernzerhof version of the generalized gradient approximation,[20] using a plane-wave basis set and a pseudopotential scheme. As the electronic coupling to the lattice is important in bismuth, we have decided to study bismuth at the theoretical lattice parameters, at variance with previous works.

The spin-orbit coupling is very important in bismuth and has been included in our calculations. We have used the full Dirac Hamiltonian near the atomic cores.[21,22] Our approach is expected to improve the description of elements as heavy as Bi. The electronic wave functions were expanded in plane waves up to a kinetic energy cutoff of 150 Ry. As only a few calculations with the full relativistic effects for bismuth exist in the literature, details about our pseudopotential and the BZ sampling are given in Appendix A.

In principle, quasiparticle theory beyond DFT, like the *GW* method,[23] should be applied to describe the electronic band structure. Moreover, after an excitation, the electron-hole interaction should be treated with the Bethe-Salpeter equation.[23] In anterior studies, we have found that although the band gap of semiconductors is grossly underestimated, the DFT description of the relative positions of the minima in the conduction band[24–26] and effective masses[26] are sufficient for our purpose.

Besides the large splitting of the *p* bands by the spin-orbit coupling, the peculiarity of the band structure of semimetallic bismuth is the overlap between the highest valence band and the lowest conduction band, which creates a Fermi surface composed of one small electron pocket at point *L* and one hole pocket at point *T*. In the full BZ there are three electron pockets and one hole pocket.

Many band structure calculations of Bi have been carried out, using different theoretical methods. Among them are the full-potential linear muffin tin orbital (FP-LMTO) approach,[27] tight-binding calculations,[28–31] and empirical pseudopotential calculations[32] which rely on a fit with experimental data. Other studies[33,34] based on DFT have fixed the occupancy of valence states before including the spin-orbit coupling. We give a detailed comparison of the energy dispersion between our relativistic scheme and previous studies in Appendix B.

As can be seen in Fig. 2, our *ab initio* calculations reproduce the subtleties around the Fermi level. It turns out that the carrier pockets at the Fermi level are satisfactorily reproduced with the GGA (Table II, lines 1–3). An extremely good agreement is also found for the valence band at Γ when comparing our GGA results with the photoemission data[36] (Table II, lines 4,5,8). We have checked also the LDA exchange and correlation functional. At the experimental lattice parameters, which are very close to the LDA equilibrium ones, our results are close to those of Ref. 27. The agreement with the experiment is, however, poorer than in the GGA at the GGA equilibrium lattice parameters (see, e.g., Table II, line 4). However, we point out that the LDA and GGA energy dispersions are found to be very close when the same lattice parameters are used in both calculations.

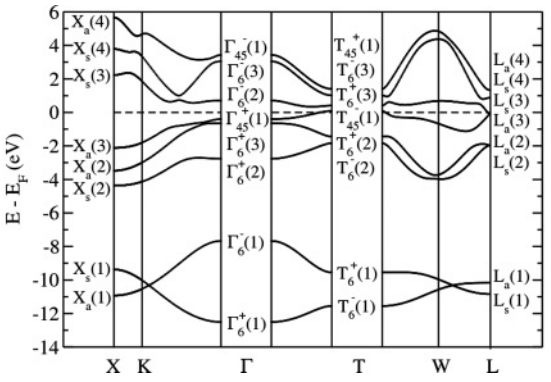

FIG. 2. Dispersion of the GGA Kohn-Sham energy bands of Bi along different high-symmetry directions in the Brillouin zone. The zero of energy is taken to be the Fermi level. The notation is as in Refs. 32 and 35.

III. EXPERIMENT

A. Setup

The terahertz spectrometer is driven by a Ti:sapphire laser oscillator delivering 10-fs pulses at a 780-nm center wavelength. Part of the laser output is used to excite the sample with an incident fluence of about 10 μJ cm^{-2}. The terahertz pulses are obtained from the residual 10% of the laser output by difference-frequency generation in a 90-μm GaSe crystal. The time-dependent terahertz electric field is detected by electro-optic sampling using the 12-fs pulses of the seed laser and a 300-μm-thick ZnTe crystal. As shown in Fig. 3, the terahertz pulses have a duration of 100 fs, covering a spectral range from 10 to 30 THz. The sample is a polycrystalline Bi film that was evaporated onto a diamond substrate. We have measured the terahertz electric field $E(t)$, transmitted through the sample in thermodynamic equilibrium at an ambient temperature. Repeating the measurement for different delays τ provides the change $\Delta E(t,\tau)$ in the transmitted electric field induced by the pump pulse. Here t denotes the time of the terahertz pulse with respect to the field maximum at $t = 0$, and τ is the pump-probe delay.

Typical terahertz waveforms are shown in Fig. 3. $E(t)$ is the electric field transmitted through the unexcited bismuth film, and $\Delta E(t,\tau)$ is the pump-induced change at time $\tau = 100$ fs after the excitation. In addition, we have measured the electric field $E_0(t)$ transmitted through the diamond substrate without the bismuth film (not shown). The incident and transmitted terahertz electric fields are Fourier transformed with respect to t, and the conductivity of the bismuth film is then obtained by inverting the Fresnel formulas.

In the limit of small film thickness, the dielectric function of bismuth reads

$$\varepsilon(\omega) = \left(\frac{E_0(\omega)}{E(\omega)} - 1\right)\frac{c}{i\omega d}(n+1), \tag{1}$$

and the pump-induced change of the dielectric function is

$$\Delta\varepsilon(\omega,\tau) = \frac{\Delta E(\omega,\tau)}{E(\omega)}\frac{c}{i\omega d}\left(n+1+\frac{\omega d}{ic}\varepsilon(\omega)\right). \tag{2}$$

Here n is the refractive index of the diamond substrate, c is the light velocity, d is the film thickness, and ω is the frequency of the terahertz probe. We would like to point out that terahertz spectroscopy enables us to determine the dielectric properties of a material without relying on Kramers-Kronig relations.

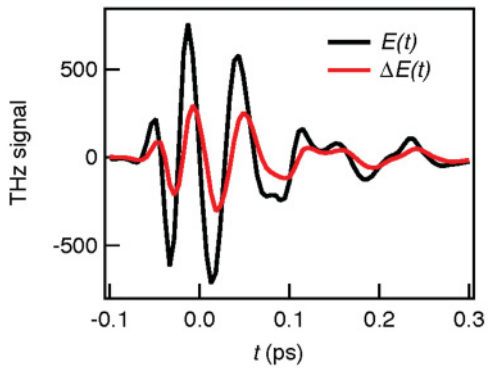

FIG. 3. (Color online) The electric field transmitted through the unexcited bismuth film, $E(t)$ (dark line), and the pump-induced change $\Delta E(t,\tau)$ at $\tau = 100$ fs (red line).

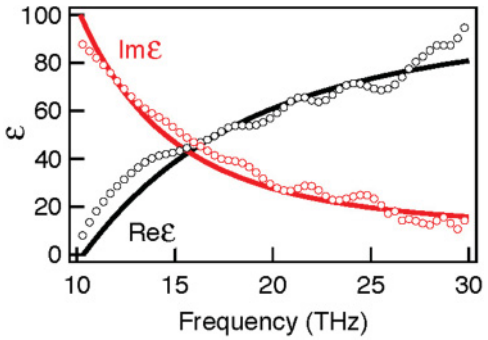

FIG. 4. (Color online) The equilibrium dielectric function $\varepsilon(\omega)$, measured as a function of frequency (circles) and the result of a fit with the Drude model (solid lines).

B. Dielectric properties at equilibrium

Figure 4 shows the equilibrium dielectric function $\varepsilon(\omega)$ and the result of a fit obtained with the Drude model:

$$\varepsilon(\omega) = -\frac{\omega_p^2}{\omega(\omega+i\gamma)} + \varepsilon_\infty. \tag{3}$$

We obtain as best-fitting values the plasma frequency $\hbar\omega_p = 560$ meV, scattering rate $\hbar\gamma = 37$ meV, and $\varepsilon_\infty = 100$. The reasonably good fit achieved with the Drude model confirms that free carriers dominate $\varepsilon(\omega)$ in the mid-infrared spectral region. In the framework of the linear response theory, the Drude response originates from intraband optical transitions, and the absorption of a photon is accompanied by the scattering of a charge carrier with impurities, phonons, or other charge carriers.[37] In principle, two additional effects may cause deviations from a simple Drude model. First, the interband optical transitions have an absorption onset at 67 meV (16 THz) and should induce additional absorption in the mid-infrared window. However, optical measurements on an extended energy range suggest that the contribution from this term is negligible.[11] Second, the coupling of single particles to plasmonic excitations results in a temperature-dependent plasmaronic absorption.[11] Within the extended Drude model, this many-body correction induces a strong dependence of the effective scattering rate on the probing frequency. In our films, this relative variation of the scattering rate is reduced by the presence of strong extrinsic scattering. As a consequence we could accurately reproduce the imaginary part of the dielectric function by a constant scattering rate. On the other hand, a nonresonant contribution to the real part of the dielectric function results in a frequency-independent offset ε_∞. We note that the scattering rate and the plasma frequency obtained from the Drude model are larger than the values measured for single crystals of bismuth. According to Armitage *et al.*[12] the plasma frequency and scattering rate of crystalline bismuth are 400 and 5 meV, respectively. We ascribe this discrepancy to the granular structure of our polycrystalline film. Due to the presence of metallic surface states, the grain boundaries enhance the density of electronic states at the Fermi level.[10]

Moreover, the high concentration of scattering centers reduces the mean free path of the charge carriers down to 100 nm. Despite this fact, we expect all our findings on the charge carrier dynamics to be qualitatively valid also for bismuth single crystals.

C. Dielectric properties in photoexcited bismuth

The pump-induced change of the dielectric function at several delays is reported in Fig. 5. Since the Drude model accurately fits the experimental data, we conclude that the nonequilibrium distribution function of charge carriers also displays a free-carrier response. The large amplitude of the photoinduced signal is due to the relatively low density of electronic states at the Fermi level. As a consequence, the photoinduced redistribution of the occupation numbers leads to a large increase in the number of conducting carriers. Note in Fig. 5 that the measured $\Delta\varepsilon(\omega,\tau)$ first increases until about $\tau = 1$ ps and afterward decreases for larger pump-probe delays. Such a nonmonotonic dynamics is not observed in other semimetals like graphite,[2] which instead display a continuous decrease of the photoinduced signal. We verified that the temporal evolution of the terahertz signal does not show any sign of periodic oscillations due to the coherent A_{1g} mode. Usually, such a coherent phonon affects the optical spectral region by modulating the joint density of the electronic states and consequently can be observed in optical reflectivity experiments.[3,4] Here, the lack of oscillations in the temporal evolution of the terahertz signal indicates that the transient change of the nuclear positions has a negligible effect on the photoinduced plasma frequency. Simple considerations of the magnitude of the lattice movement induced by our laser field support this conclusion. According to time-resolved x-ray experiments, a laser pulse of 3 mJ/cm^2 shifts the A_{1g} coordinate by 6 pm.[5] Scaling this value with respect to the pump fluence of our experiment (10 μJ/cm^2), we estimate a photoinduced displacement of 0.02 pm. Since the isothermal compressibility of bismuth is 0.0317 GPa^{-1}, an applied pressure of 40 bar would induce a displacement of comparable amplitude. The direct comparison to the data of Armitage *et al.* suggests that such a pressure should change the plasma frequency by $\sim$1 meV.[12] This indicates that the photoinduced activation of the A_{1g} mode has minor effects on the plasma frequency. Instead, the terahertz response is strongly dominated by an $\simeq$100 times larger increase of plasma frequency, which is induced by the nonequilibrium distribution of the photoexcited electrons.

In Figs. 6(a) and 6(b), we show the evolution of the squared plasma frequency ω_p^2, and of the Drude scattering rate γ,

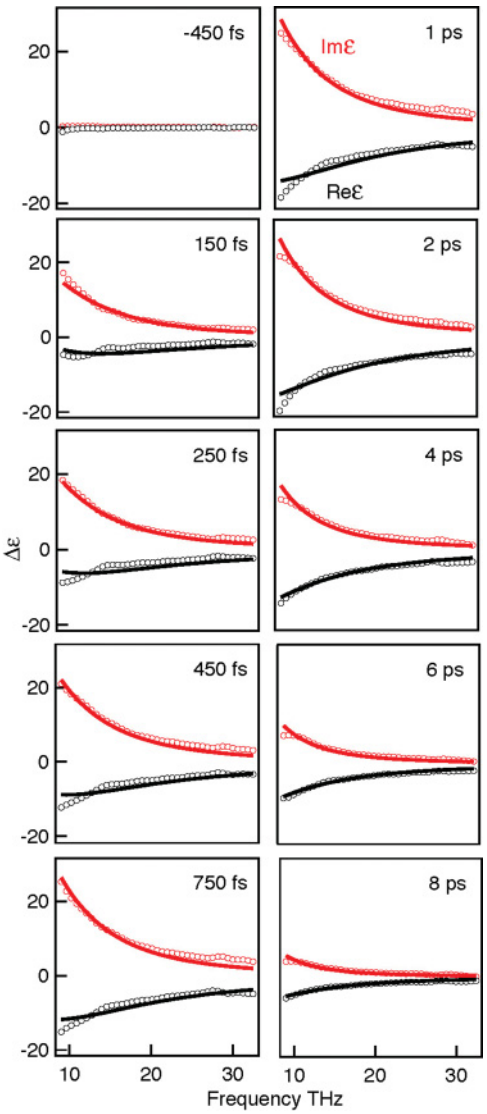

FIG. 5. (Color online) Pump-induced change of the dielectric function $\Delta\varepsilon(\omega,\tau)$ at several pump-probe delays (circles). In each panel, the upper (lower) curve is the imaginary (real) part of the variation of the dielectric function. Fits obtained with the Drude model (solid lines) are superimposed onto the experimental data.

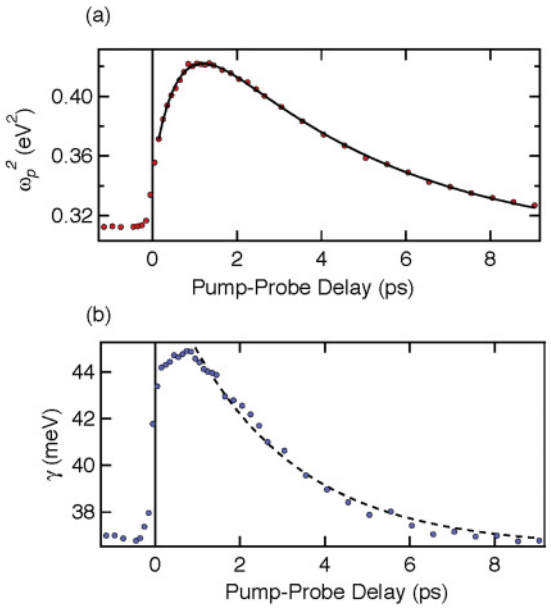

FIG. 6. (Color online) (a) Squared plasma frequency as a function of the pump-probe delay (circles). The solid line superimposed onto the experimental data is the result of a fit based on Eq. (8). (b) Drude scattering rate as a function of the pump-probe delay (circles) and exponential fit (dashed line).

as a function of the pump-probe delay τ. The value of the square of the plasma frequency is 0.31 eV^2 at equilibrium and increases up to 0.37 eV^2 just after photoexcitation. It reaches the maximum value of 0.42 eV^2 for a pump-probe delay of 1 ps, and decays exponentially at larger delays.

IV. DISCUSSION

We attribute the nonmonotonic temporal evolution of the plasma frequency to the presence of local extrema with large effective masses in the electronic band structure of bismuth. While residing in these extrema, the trapped carriers barely respond to the terahertz field. Conversely, the energy states near the Fermi level E_F have high band velocities and strongly contribute to the Drude conductivity.

In the following, the existence of local extrema in the valence and conduction bands of bismuth will be checked with calculations within the DFT and GGA. In order to interpret our experimental findings, we have investigated the possible intermediate states of the electronic system after an optical excitation of 1.6 eV. As shown in Fig. 7, the direct optical transitions generated by the pump beam promote electrons to highly excited states. Due to carrier-carrier and carrier-phonon scattering, the excited electrons and holes redistribute their internal energy. We have found that the calculated effective mass of local extrema, and in particular of a local maximum at Γ in the valence band, is much larger than the optical mass of carriers near the Fermi level (near the L and T points). The decay out of this maximum is probably dominating the initial rise of the plasma frequency.

A. Carrier mass in the valence and conduction bands

As a true local (TL) maximum (minimum) we define the top (bottom) of a valley where the energy band is at an extremum along three principal axes. We have investigated the full BZ with the precision of $\Delta k = 0.026(2\pi/a_0)$ and found six TL extrema involved in the photoexcitation process. Three of them are maxima, at the points Γ, T, and L. The energy value of the maximum at T lies above the Fermi level, while maxima at Γ and L lie below the Fermi level. Two minima

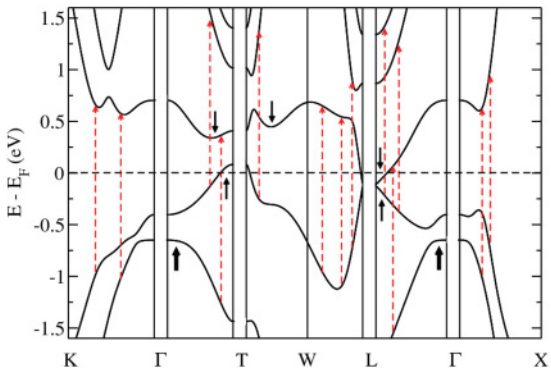

FIG. 7. (Color online) Zoom on the local extrema in the valence and conduction bands near the Fermi level. The black arrows indicate the true local extrema found in the high-symmetry directions, whereas the red dashed arrows stand for the direct optical excitations of 1.6 eV induced by the pump beam.

TABLE I. Effective mass tensor expressed in terms of the principal axes for the maxima and minima involved in the terahertz experiment. $\langle m^* \rangle$ is the average effective mass defined as $\langle m^* \rangle^{-1} = (m_1^{*-1} + m_2^{*-1} + m_3^{*-1})/3$. The unit is the free-electron mass m_0.

	m_1^*	m_2^*	m_3^*	$\langle m^* \rangle$
		Maxima		
Γ	48.1	48.1	8.1	18.1
T	0.06	0.06	0.85	0.08
L	0.003	0.27	0.005	0.006
		Minima		
T-Γ	0.14	0.14	1.50	0.20
T-W	0.94	0.04	2.44	0.11
L	0.003	0.29	0.005	0.006

lie above the Fermi level, in the lowest conduction band along high-symmetry directions, close to the T point (their positions are given in Ref. 38). The remaining minimum lies at the L point, below the Fermi level. These six extrema are indicated in Fig. 7 by black arrows. Their effective mass tensors have been computed as $[m^{*-1}(\mathbf{k})]_{ij} = \hbar^{-2}\partial^2 E(\mathbf{k})/(\partial k_i \partial k_j)$, $i,j = \overline{1,3}$, and the values are reported in Table I. The effective masses of the hole pocket at the T point and of the electron pockets at L points are in good agreement with those in Refs. 31 and 39–41.

The average mass of the maximum at Γ is strikingly large, $\langle m_h^* \rangle = 18.1 m_0$, where h stands for heavy carriers, and is approximatively two orders of magnitude larger than the average effective masses at the other extrema (Table I). The existence of the maximum at Γ turns out to be robust: for instance, when evaluated at a hydrostatic pressure of 10 kbar, the extremum is still located at the Γ point, and the value of the average effective mass is larger ($64 m_0$).

We have also computed the optical masses of carriers probed in our experiment at the L and T points, m_l^{op} (l stands for light carriers). We have obtained the optical mass by calculating independently within the DFT the number of pump-induced carriers Δn_l and the change in the plasma frequency $\Delta\omega_p^2$ due to the photoexcitation. Then the relationship between these two quantities is obtained by applying the Drude law. We recall that the number of pump-induced carriers and the change in the plasma frequency at the L (T) point read

$$\Delta n_l(T) = \int g(E)|f(E,T_0) - f(E,T)|dE, \qquad (4)$$

$$\Delta\omega_p^2(T) = 4\pi e^2 v_F^2 \int g(E)[f'(E,T_0) - f'(E,T)]dE, \qquad (5)$$

where $g(E)$ is the density of carrier states restricted to the region in reciprocal space around the L (T) point, $f(E,T)$ is the Fermi-Dirac distribution at the electronic temperature T, $f'(E,T)$ is its derivative with respect to E at the electronic temperature T, $T_0 = 300$ K is the temperature in our experiments, and v_F is the Fermi velocity of light carriers. Our determination of the plasma frequency agrees with that of Ref. 42 but for the fact that we calculate it at a finite temperature. We defer the description of details of the computation of m_l^{op} to a separate presentation. We have found the following values: $m_l^{op}(\mathrm{T}) \approx 0.2 m_0$ for the carrier mass at T, and $m_l^{op}(\mathrm{L}) \approx 0.05 m_0$ for the carrier mass at L. These optical masses are much smaller than the average effective masses of

holes at the local maximum in the valence band at Γ. The latter thus acts as a reservoir for the holes and slows down the hole thermalization process.

B. Temporal evolution of the plasma frequency

Our DFT calculations confirm the conjecture that light carriers at the Fermi level, at the T and L points, strongly dominate the terahertz response. Instead, the local extrema, in particular the maximum at Γ, act as reservoirs of heavy carriers where they spend a fraction of a picosecond before relaxing to the Fermi level. As a consequence, we expect that two characteristic time scales determine the temporal evolution of the photoexcited carriers: (a) the holes residing in the local maximum decay into higher-energy states near the T point with a rate $1/\tau_h$ and (b) the electron-hole plasma at the Fermi level recombines with a rate $1/\tau_l$.

The simplest model accounting for such a dynamics is described by the rate equations

$$\frac{\partial n_h}{\partial t} = -\frac{n_h}{\tau_h}, \tag{6}$$

$$\frac{\partial \Delta n_l}{\partial t} = -\frac{\Delta n_l}{\tau_l} + \frac{\lambda n_h}{\tau_h}, \tag{7}$$

of which the solution is

$$\Delta n_l(t) = \left(\Delta n_l^0 - \frac{\lambda n_h^0}{\tau_h/\tau_l - 1}\right) e^{-t/\tau_l} + \frac{\lambda n_h^0}{\tau_h/\tau_l - 1}\, e^{-t/\tau_h}. \tag{8}$$

Here $n_h(t)$ is the number of heavy carriers in the local extrema, $\Delta n_l(t)$ is the change of the number of light carriers near the Fermi level, and n_h^0 and Δn_l^0 are the values of $n_h(t)$ and $\Delta n_l(t)$ just after photoexcitation, respectively. The parameter λ is the carrier multiplication factor accounting for secondary electron-hole pairs generated by impact ionization.[43,44] In our experiment, we only probe $\Delta n_l(t)$, which is proportional to the pump-induced change in the plasma frequency squared, $\Delta\omega_p^2(t)$. We show in Fig. 6(a) the curve obtained with the best-fitting parameters $\tau_h = 0.6 \pm 0.1$ ps, $\tau_l = 4.0 \pm 0.5$ ps, and $\lambda n_h^0/\Delta n_l^0 = 2.24 \pm 0.5$. The value of λ depends on the relative weights of impact ionization, Auger recombination, and carrier-phonon scattering. If the photoexcited carriers decayed solely by phonon emission, the number of carriers would be conserved. On the other hand, the carrier multiplication factor should be larger than 1 when the carrier-carrier interaction dominates the thermalization process. Simulations on photoexcited graphene,[43] and experiments on PbSe,[44] suggest that $1 < \lambda < 2$ for an excitation with photon energy of 1.5 eV. According to this estimation, a consistent fraction of the holes created during photoexcitation of bismuth populates the local extrema soon after the photoexcitation.

The reported time scale of $\tau_h = 0.6$ ps is comparable to the electron-phonon intervalley scattering time observed in semiconductors.[25,45–47] Note that the recombination of the electron-hole plasma at the T and L points is a slower process ($\tau_l = 4$ ps). A similar time scale has also been observed in the recovery time of transient conductivity.[4] Such an inefficient cooling of the plasma is due to the semimetallic density of states, which reduces the number of final states available for the electron-phonon and hole-phonon scattering.

We show in Fig. 6(b) the result of the fit of the Drude scattering rate γ as a function of the pump-probe delay. The sudden increase of γ in the photoexcited state is due to the larger phase space that becomes available for scattering events. Note that γ slightly increases during the first picosecond, and decreases exponentially at longer delays with a time constant of 2.6 ps. It follows that the scattering rate decreases almost twice as fast as the carrier density. On the other hand, we notice that the carrier scattering is dominated by the large defect concentration in our polycrystalline films. Further experiments on high-quality single crystals would be necessary in order to observe the behavior of the intrinsic scattering channels.

V. CONCLUSIONS

Our time-resolved terahertz experiment and *from-first-principles* calculations provide insights into the carrier distribution function soon after photoexcitation in bismuth. It follows that most of the primary holes spend several hundreds of femtoseconds in the local extremum at Γ of the band structure. The calculated effective mass of that maximum, $\langle m_h^* \rangle = 18.1 m_0$, is much larger than the optical mass of carriers near the Fermi level. The decay of such heavy holes to states close to the Fermi level takes place with an inverse rate of 0.6 ps. Such a decay mechanism is similar to the intervalley scattering observed in many semiconductors. As a consequence, the complete thermalization of the electron-hole plasma takes place on a time scale larger than a phonon period. This result should be taken into account in models that attempt a description of the coherent phonon generation and phonon softening in photoexcited bismuth. Finally, we would like to point out that our experiments have been carried out in the regime of low excitation densities ($\approx 10^{-4}$ electrons per unit cell). Since we expect the dynamics of electrons to be fluence dependent, further investigations at higher excitation densities would be necessary to reproduce the conditions employed in time-resolved x-ray diffraction and time-resolved photoemission experiments.

ACKNOWLEDGMENTS

We thank T. Cornelius for providing us with bismuth samples that were useful for the experiment. The calculations were performed using the QUANTUM ESPRESSO package.[48] The pseudopotential was generated with the help of A. Dal Corso, with the ATOMIC code in the QUANTUM ESPRESSO package. Figure 1 was produced using XCRYSDEN.[49] We thank A. Dal Corso, B. Arnaud, A. Gellé, and J. Sjakste for fruitful discussions. Support from the ANR (Project No. PNANO ACCATTONE) and from DGA are gratefully acknowledged. Computer time was granted by GENCI (Project No. 2210).

APPENDIX A: COMPUTATIONAL DETAILS

We have generated a fully relativistic norm-conserving pseudopotential (PP) in a separable form,[50] using the Troullier-

Martins method.[51] The spin-orbit coupling arises in the $\mathbf{L}\cdot\mathbf{S}$ form.[52] The external electron configuration of Bi is $6s^26p^3$, plus a complete $5d$ shell. These s and p levels form energy bands in the solid, while the other d-electron and core-electron energy levels remain practically unchanged. Nevertheless, we have included d levels in the valence bands (as in Ref. 53, and at variance with Ref. 34), because of its influence on the exchange energy, which shows up in the transferability tests of the pseudopotential. The tests of transferability of the pseudopotential are remarkably improved when $5d$ states are included in the valence bands.

The electronic configuration of the neutral atom $[\mathrm{Xe}]4f^{14}5d^{10}6s^26p^3$, has been chosen as the reference for our PP. The $5d$, $6s$, and $6p$ pseudopotentials have been set up with matching radii of 1.88, 1.79, and 2.30 a.u., respectively, and the PP of unoccupied $5f$ levels with a 2.41 a.u. matching radius. In the solid, the s channel has been chosen to be the local part of the PP. No ghost states have been detected.

The calculations have been converged with respect to all of the parameters, and special attention has been paid to the BZ sampling. The self-consistent Kohn-Sham potential, the dispersion of the Kohn-Sham energy levels, and the carrier masses have been calculated with a $20\times20\times20$ **k**-point mesh centered at the Γ point, yielding 781 **k** points in the irreducible part of the BZ. We have used the Methfessel-Paxton smearing method[54] with a broadening parameter σ equal to 0.02 Ry. Special attention has been paid to the convergence of the Fermi energy: it has been obtained independently by a calculation with the improved tetrahedron method of Ref. 55 with a $50\times50\times50$ **k**-point mesh centered at the Γ point, and the energy levels of the lowest $5d$ state have been aligned in the two calculations. A precision of ±5 meV on E_F has been achieved.

APPENDIX B: KOHN-SHAM ENERGY BANDS

With our pseudopotential, we have performed *ab initio* calculation of the dispersion of Kohn-Sham eigenvalues at the theoretical lattice parameters, at variance with the calculations of Refs. 34 and 27. Details of the band structure around the Fermi levels are subtle: we have found that without spin-orbit coupling, the hole pocket would not be present at the T point, confirming Ref. 34.

In Table II, we report the values of characteristic energy levels obtained with our pseudopotential, the FP-LMTO method,[27] the tight-binding methods,[31] the DFT approach,[33,34] and experiments. To summarize, we have obtained the following values:

(i) the energy difference of the two highest occupied bands at the L point, $E[L_a(3)]-E[L_s(3)]=-24$ meV (Table II, line 1);

(ii) the energy difference of the two lowest unoccupied bands at the T point, $E[T_6^+(3)]-E[T_{45}^-(1)]=326$ meV (Table II, line 2);

(iii) the overlap energy $E[T_{45}^-(1)]-E[L_s(3)]=188$ meV between the top of the band crossing the Fermi level (BCFL) at the T point and the bottom of the BCFL at the L point (Table II, line 3);

(iv) energy levels at the Γ and T points that are in remarkable agreement with the photoemission experiment of Ref. 36 (Table II, lines 4,5,8).

Our value of the overlap energy is somewhat overestimated (Table II, line 3). The quasiparticle theory should be applied to describe energy differences between occupied and unoccupied levels. We point out that none of the calculations of Refs. 31, 33, and 34 includes spin-orbit coupling self-consistently. The accuracy of our calculation shown in Table II is sufficient for our purpose.

TABLE II. Energy levels (eV) as obtained in this work in the GGA, in other calculations (Refs. 27, 31, and 34) and in experiments (Refs. 31 and 36).

	This	Theory			Expt.	
Band energy	work	Ref.[a]	Ref.[b]	Ref.[c]	Ref.[d]	Ref.[e]
$L_a(3)-L_s(3)$	-0.024		-0.262	-0.014		-0.011–-0.015
$T_6^+(3)-T_{45}^-(1)$	0.326		0.467	0.370		0.18–0.41
$T_{45}^-(1)-L_s(3)$	0.188	0.163	0.041	0.038		0.036–0.039
$\Gamma_6^-(1)-\Gamma_6^+(1)$	4.82	5.61	5.73	5.91	4.7	5.9
$\Gamma_{45}^+(1)-\Gamma_6^+(3)$	0.25	0.23	0.19	0.31	0.35	
$\Gamma_6^-(2)-\Gamma_{45}^+(1)$	1.11		1.72	1.07		0.72–0.81
$\Gamma_6^-(2)-\Gamma_6^+(3)$	1.35		1.91	1.37		0.65–0.71
$T_6^+(1)-T_6^-(1)$	2.01	1.94	1.88	1.11	1.9	1.18
$T_6^+(2)-T_{45}^-(1)$	-1.52	-2.08	-1.30	-1.13		
$T_6^-(3)-T_{45}^-(1)$	0.94		1.09	0.94		0.80–0.88
$L_a(1)-L_s(1)$	0.67		0.72	0.36		
$L_a(2)-L_s(3)$	-1.86		-1.97	-1.64		-1.92–-2.10
$L_s(4)-L_a(3)$	1.00		1.04	0.84		1.05–1.15
$L_s(4)-L_s(3)$	0.97		0.78	0.83		

[a]Shick *et al.*, Ref. 27.
[b]Gonze *et al.*, Ref. 34, cited in Ref. 30.
[c]Liu *et al.*, Ref. 31.
[d]From Ref. 36. Accuracy on one single level was 0.25 eV.
[e]From Table IV of Ref. 31.

[1] H. J. Zeiger, J. Vidal, T. K. Cheng, E. P. Ippen, G. Dresselhaus, and M. S. Dresselhaus, Phys. Rev. B **45**, 768 (1992).
[2] T. Kampfrath, L. Perfetti, F. Schapper, C. Frischkorn, and M. Wolf, Phys. Rev. Lett. **95**, 187403 (2005).
[3] M. Hase, M. Kitajima, S. I. Nakashima, and K. Mizoguchi, Phys. Rev. Lett. **88**, 067401 (2002).
[4] K. Ishioka, M. Kitajima, and O. Misochko, J. Appl. Phys. **100**, 093501 (2006).
[5] D. Fritz, D. Reis, B. Adams, R. Akre, J. Arthur, C. Blome, P. Bucksbaum, A. Cavalieri, S. Engemann, S. Fahy *et al.*, Science **315**, 633 (2007).
[6] S. L. Johnson, P. Beaud, E. Vorobeva, C. J. Milne, E. D. Murray, S. Fahy, and G. Ingold, Phys. Rev. Lett. **102**, 175503 (2009).
[7] E. S. Zijlstra, L. E. Díaz-Sánchez, and M. E. Garcia, Phys. Rev. Lett. **104**, 029601 (2010).
[8] Y. Giret, A. Gellé, and B. Arnaud, Phys. Rev. Lett. **106**, 155503 (2011).
[9] M. Muntwiler and X.-Y. Zhu, New J. Phys. **10**, 113018 (2008).
[10] Y. M. Koroteev, G. Bihlmayer, J. E. Gayone, E. V. Chulkov, S. Blügel, P. M. Echenique, and P. Hofmann, Phys. Rev. Lett. **93**, 046403 (2004).
[11] R. Tediosi, N. P. Armitage, E. Giannini, and D. van der Marel, Phys. Rev. Lett. **99**, 016406 (2007).
[12] N. P. Armitage, R. Tediosi, F. Lévy, E. Giannini, L. Forro, and D. van der Marel, Phys. Rev. Lett. **104**, 237401 (2010).
[13] M. Cohen, Phys. Rev. **121**, 387 (1961).
[14] R. D. Brown, R. L. Hartman, and S. H. Koenig, Phys. Rev. **172**, 598 (1968).
[15] R. J. Needs, R. M. Martin, and O. H. Nielsen, Phys. Rev. B **33**, 3778 (1986).
[16] L. Falicov and S. Golin, Phys. Rev. **137**, A871 (1965).
[17] D. Schiferl and C. Barrett, J. Appl. Crystallogr. **2**, 30 (1969).
[18] P. Hohenberg and W. Kohn, Phys. Rev. **136**, B864 (1964).
[19] W. Kohn and L. Sham, Phys. Rev. **140**, A1133 (1965).
[20] J. P. Perdew, K. Burke, and M. Ernzerhof, Phys. Rev. Lett. **77**, 3865 (1996).
[21] A. Dal Corso, Phys. Rev. B **76**, 054308 (2007).
[22] A. Dal Corso, Phys. Rev. B **82**, 075116 (2010).
[23] G. Onida, L. Reining, and A. Rubio, Rev. Mod. Phys. **74**, 601 (2002).
[24] F. Bruneval, N. Vast, and L. Reining, Phys. Rev. B **74**, 045102 (2006).
[25] J. Sjakste, N. Vast, and V. Tyuterev, Phys. Rev. Lett. **99**, 236405 (2007).
[26] V. G. Tyuterev, S. V. Obukhov, N. Vast, and J. Sjakste, Phys. Rev. B **84**, 035201 (2011).
[27] A. B. Shick, J. B. Ketterson, D. L. Novikov, and A. J. Freeman, Phys. Rev. B **60**, 15484 (1999).
[28] S. Mase, J. Phys. Soc. Jpn. **13**, 434 (1958).
[29] S. Mase, J. Phys. Soc. Jpn. **14**, 584 (1959).
[30] J. H. Xu, E. G. Wang, C. S. Ting, and W. P. Su, Phys. Rev. B **48**, 17271 (1993).
[31] Y. Liu and R. E. Allen, Phys. Rev. B **52**, 1566 (1995).
[32] S. Golin, Phys. Rev. **166**, 643 (1968).
[33] X. Gonze, J.-P. Michenaud, and J.-P. Vigneron, Phys. Scr. **37**, 785 (1988).
[34] X. Gonze, J.-P. Michenaud, and J.-P. Vigneron, Phys. Rev. B **41**, 11827 (1990).
[35] C. R. Ast and H. Höchst, Phys. Rev. B **70**, 245122 (2004).
[36] G. Jezequel, J. Thomas, and I. Pollini, Phys. Rev. B **56**, 6620 (1997).
[37] R. V. Baltz and W. Escher, Phys. Status Solidi B **51**, 499 (1972).
[38] The minimum along the Γ-T direction is located 0.25 Å^{-1} from the T point ($E - E_F = 0.34$ eV), and the minimum along the T-W direction is located 0.29 Å^{-1} from the T point ($E - E_F = 0.45$ eV).
[39] J.-P. Issi, Aust. J. Phys. **32**, 585 (1979).
[40] R. Isaacson and G. Williams, Phys. Rev. **185**, 682 (1969).
[41] G. Smith, G. Baraff, and J. Rowell, Phys. Rev. **135**, A1118 (1964).
[42] T. Pedersen, P. Modak, K. Pedersen, N. Christensen, M. Kjeldsen, and A. Larsen, J. Phys.: Condens. Matter **21**, 115502 (2009).
[43] T. Winzer, A. Knorr, and E. Malic, Nano Lett. **10**, 4839 (2010).
[44] J. Pijpers, R. Ulbricht, K. Tielrooij, A. Osherov, Y. Golan, C. Delerue, G. Allan, and M. Bonn, Nat. Phys. **5**, 811 (2009).
[45] J. Cockburn, J. Finley, M. Skolnick, P. Wisniewski, R. Grey, G. Hill, and M. Pate, Appl. Phys. Lett. **70**, 622 (1997).
[46] S. Wu, P. Geiser, J. Jun, J. Karpinski, D. Wang, and R. Sobolewski, J. Appl. Phys. **101**, 043701 (2007).
[47] M. C. Beard, G. M. Turner, and C. A. Schmuttenmaer, Phys. Rev. B **62**, 15764 (2000).
[48] P. Giannozzi, S. Baroni, N. Bonini, M. Calandra, R. Car, C. Cavazzoni, D. Ceresoli, G. Chiarotti, M. Cococcioni, I. Dabo *et al.*, J. Phys.: Condens. Matter **21**, 395502 (2009).
[49] A. Kokalj, J. Mol. Graphics Modell. **17**, 176 (1999), code available from http://www.xcrysden.org/.
[50] L. Kleinman and D. M. Bylander, Phys. Rev. Lett. **48**, 1425 (1982).
[51] N. Troullier and J. L. Martins, Phys. Rev. B **43**, 1993 (1991).
[52] G. B. Bachelet, D. R. Hamann, and M. Schlüter, Phys. Rev. B **26**, 4199 (1982).
[53] G. Gutiérrez and E. Menéndez-Proupin, J. Appl. Phys. **99**, 103504 (2006).
[54] M. Methfessel and A. T. Paxton, Phys. Rev. B **40**, 3616 (1989).
[55] P. E. Blöchl, O. Jepsen, and O. K. Andersen, Phys. Rev. B **49**, 16223 (1994).